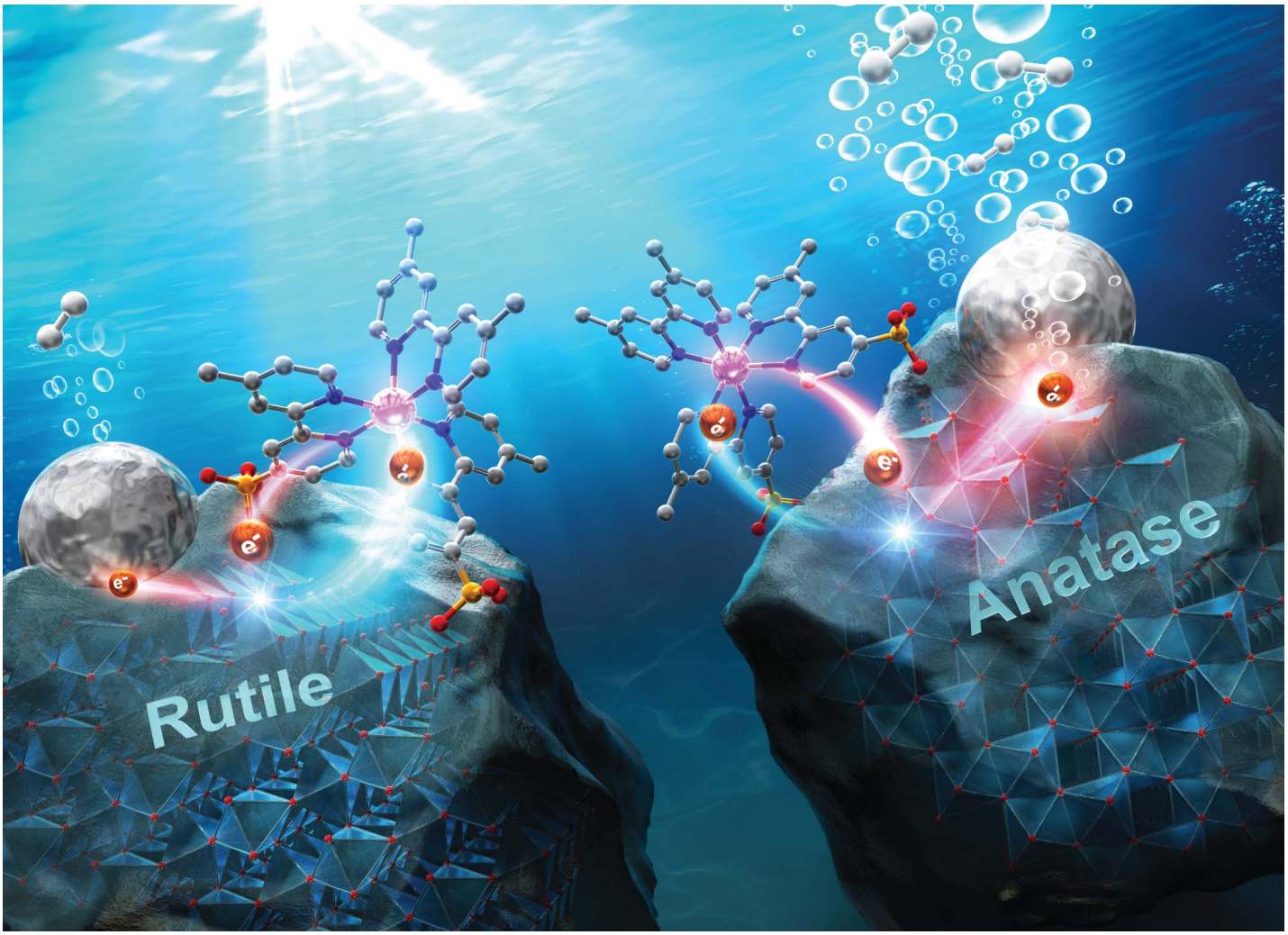

Showcasing research from Professor Kazuhiko Maeda's laboratory, School of Science, Institute of Science Tokyo, Japan.

Visible-light H_2 evolution using dye-sensitized TiO_2: effects of physicochemical properties of TiO_2 on excited carrier dynamics and activity

Shining light on Ru(II)-dye–sensitized TiO_2, we reveal how crystal phase controls interfacial charge transfer and visible-light H_2 evolution. Both rutile and anatase allow efficient electron injection from the excited state dye, but faster back electron transfer from TiO_2 to dye suppresses activity in rutile. In contrast, anatase outperforms by sustaining charge separation, driving more efficient H_2 evolution.

Image reproduced by permission of Kazuhiko Maeda from *J. Mater. Chem. A*, 2025, **13**, 36997.

As featured in:

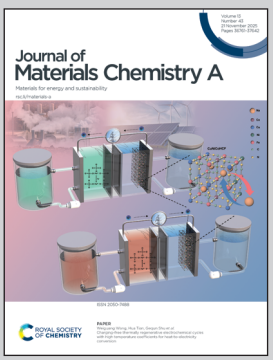

See Thomas E. Mallouk, Kazuhiko Maeda *et al.*, *J. Mater. Chem. A*, 2025, **13**, 36997.

ROYAL SOCIETY OF CHEMISTRY

rsc.li/materials-a

Registered charity number: 207890

Journal of Materials Chemistry A

ROYAL SOCIETY OF CHEMISTRY

PAPER

View Article Online
View Journal | View Issue

Cite this: J. Mater. Chem. A, 2025, 13, 36997

Visible-light H_2 evolution using dye-sensitized TiO_2: effects of physicochemical properties of TiO_2 on excited carrier dynamics and activity

Kakeru Harada,[a] Haruka Yamamoto,[a] Megumi Okazaki,[a] Thomas E. Mallouk *[b] and Kazuhiko Maeda *[ac]

Dye-sensitized photocatalysts have emerged as promising materials for solar-driven water splitting due to their ability to utilize visible light, in contrast to conventional wide-band-gap semiconductors. However, the relationship between semiconductor properties and charge carrier dynamics remains insufficiently understood. In this study, we investigated Pt/TiO_2 systems sensitized with a visible-light-absorbing Ru(II) polypyridyl complex (**RuP**), focusing on how the crystal phase and specific surface area of TiO_2 influence excited carrier dynamics and H_2 evolution activity. To isolate the effects of TiO_2 properties, Pt and **RuP** loadings were standardized across samples. Emission lifetime analysis showed similarly efficient electron injection from **RuP** to TiO_2 in all cases, suggesting that injection efficiency does not account for observed differences in activity. Transient absorption measurements revealed that back electron transfer (BET) rates depended strongly on the TiO_2 phase, with anatase and P25 exhibiting slower BET and higher activity for H_2 evolution than rutile. The highest apparent quantum yield for H_2 evolution was 12.0% at 450 nm. Among anatase samples, larger surface areas correlated with higher activity, while smaller-area samples exhibited slower BET rates but still low H_2 evolution activity, implying a role for **RuP** dye–dye interactions in performance loss. This was further supported by improvements in H_2 evolution activity by lowering **RuP** loading or adding co-adsorbents. Overall, these results demonstrate that both BET suppression and control over **RuP** dye aggregation are essential for designing efficient dye-sensitized photocatalytic systems.

Received 9th July 2025
Accepted 10th August 2025

DOI: 10.1039/d5ta05528h

rsc.li/materials-a

Introduction

In response to pressing global environmental issues such as global warming, the realization of a sustainable energy society is of critical importance. Among various energy carriers, H_2 has attracted considerable attention as a clean energy source, since its combustion does not release CO_2. One promising method for H_2 production is semiconductor-based photocatalytic water splitting using solar energy.[1,2] H_2 produced by this approach can serve as a medium for the storage and transport of renewable energy, contributing to the establishment of a future carbon-neutral society.

Against this background, numerous photocatalytic materials have been developed.[3–6] However, photocatalysts exhibiting high quantum yields for overall water splitting are comprised mostly of wide band gap semiconductors exceeding 3 eV,[7,8] which limits their ability to utilize visible light that constitutes the majority of the solar spectrum. To address this challenge, dye-sensitized photocatalysts have been proposed.[9,10] In these systems, visible-light-responsive dyes are adsorbed onto the surface of wide band gap semiconductors, enabling the injection of electrons from the excited dyes into the conduction band of the semiconductor under visible light irradiation, thereby driving the H_2 evolution reaction. Most dye-sensitized photocatalysts are primarily active for H_2 evolution alone; however, by employing reversible redox mediators, such as the I_3^-/I^- couple, overall water splitting based on Z-scheme designs is possible.[11–16]

While dye-sensitized photocatalysts have demonstrated their effectiveness in extending visible light absorption capability, their photocatalytic performance remains insufficient for practical application. One of the major factors limiting the efficiency is back electron transfer (BET), in which electrons injected into the conduction band of the semiconductor recombine with the oxidized dye molecules (Scheme 1).[13,17–19] While the electron injection process from the excited state dye to the semiconductor is generally very efficient,[20] the BET process competes with the desired H_2 generation reaction and

[a]Department of Chemistry, School of Science, Institute of Science Tokyo, 2-12-1-NE-2 Ookayama, Meguro-ku, Tokyo 152-8550, Japan. E-mail: maeda@chem.sci.isct.ac.jp
[b]Department of Chemistry, University of Pennsylvania, 231 S. 34th Street, Philadelphia, PA 19104, USA. E-mail: mallouk@sas.upenn.edu
[c]Research Center for Autonomous Systems Materialogy (ASMat), Institute of Science Tokyo, 4259 Nagatsuta-cho, Midori-ku, Yokohama, Kanagawa 226-8501, Japan

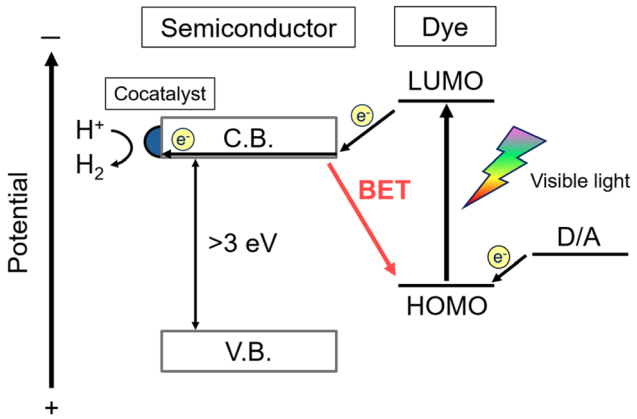

Scheme 1 Schematic energy diagram of a dye-sensitized H_2 evolution photocatalyst. C.B.: conduction band; V.B.: valence band; D: electron donor; A: electron acceptor.

constitutes a significant source of energy loss in dye-sensitized photocatalytic systems.

Research on BET has so far been mainly conducted in the field of dye-sensitized solar cells (DSSCs).[21–29] For example, it has been reported that coating the semiconductor surface with insulating materials such as alumina (Al_2O_3) can effectively suppress BET to the dye.[23] In addition, factors such as surface modification,[29] the pH of the solution,[24,26] and light intensity[21] are known to influence charge recombination processes.

Studies on DSSCs have also shown that the crystal structure of TiO_2—anatase *versus* rutile—has a strong impact on device performance.[22] In general, rutile-type TiO_2 exhibits lower short-circuit current density (J_{SC}) compared to anatase, mainly due to its lower specific surface area (SSA), which limits dye adsorption. Furthermore, since anatase has a more negative conduction band potential, it can potentially provide an enhanced driving force for the photocurrent observed in DSSCs.[25] Commercial TiO_2 materials such as P25, which contain rutile and amorphous phases in addition to the main anatase phase, have also been reported to exhibit lower dye uptake and lower performance.[30] However, it remains unclear whether these differences are solely attributable to dye adsorption, or if they are fundamentally related to crystal structure and surface properties. These findings underscore the importance of intrinsic material characteristics in controlling interfacial electron transfer. In contrast, such relationships have not been extensively investigated in dye-sensitized photocatalytic systems.

Some studies have examined photocatalytic H_2 production using different TiO_2 materials in dye-sensitized systems. For instance, the influence of SSA and surface functional group density on H_2 evolution activity was evaluated using several anatase-type TiO_2 samples and an organic dye (a binaphthol derivative).[31] In another study, comparisons of various TiO_2 samples in a Ru-complex-sensitized system showed that photocatalytic activity varied depending on support properties such as SSA.[32] While these studies provided valuable insights into how TiO_2 characteristics affect H_2 evolution efficiency, they did not delve into how these factors govern interfacial electron transfer processes.

In this study, we systematically investigated how the crystal structure and SSA of TiO_2 influence photocatalytic activity and interfacial electron transfer processes, including both BET characteristics and excited dye-to-TiO_2 electron transfer, using 14 different TiO_2 samples. By unifying the amount of adsorbed dye and the Pt cocatalyst loading across all samples, we eliminated variations arising from differences in dye coverage or cocatalyst quantity. This carefully controlled experimental design is a key feature of our study, as it allows for a direct comparison based primarily on the intrinsic physicochemical properties of TiO_2. Furthermore, by combining time-resolved emission and transient absorption spectroscopy, we dynamically observed both electron injection from the excited dye into TiO_2 and BET from TiO_2 to the oxidized dye, and clarified the relationships between the kinetics of these processes and the properties of TiO_2. As a result, we found that differences in photocatalytic activity are influenced not only by variations in dye adsorption and surface area, but also by differences in interfacial electron transfer dynamics associated with the crystal structure and surface properties of TiO_2.

This study is the first comprehensive investigation that explicitly evaluates the differences in electron transfer processes arising from intrinsic semiconductor properties, which have often been overlooked in dye-sensitized photocatalytic systems. It provides a new perspective and rational design guidelines for photocatalyst development.

Experimental

Preparation of Pt/TiO_2

The loading of Pt nanoparticles onto TiO_2 was carried out by a photodeposition method.[33] Each TiO_2 sample (300 mg) was dispersed in an aqueous methanol solution (15 vol%, 140 mL) containing $H_2PtCl_6 \cdot 6H_2O$ (≥98.5%, FUJIFILM Wako Pure Chemical Corporation) (0.10 wt% Pt *vs.* TiO_2), and irradiated for 1.5 h using a 300 W Xe lamp (Cermax, PE300BF) equipped with an CM-1 cold mirror. The irradiation was performed over an area of 44 cm^2, and the average light intensity was approximately 22.3 mW cm^{-2} (measured over the 300–410 nm range using a UV light meter, model C9536-01 with H9958-01 sensor head, Hamamatsu Photonics). After irradiation, the suspension was filtered using an Omnipore™ 0.1 μm PTFE membrane filter (47 mm, Merck Millipore), washed with water, and collected as a powder after drying at 343 K. The TiO_2 samples used in this study included the JRC-TIO series (JRC-TIO-1, 4(2), 6, 7, 8, 9, 10, 12, 13, 14, 15, 16), kindly supplied by the Catalysis Society of Japan, as well as commercially available AEROXIDE TiO_2 P25 (≥99.5%, NIPPON AEROSIL CO.) and anatase-type TiO_2 (≥99.5%, Kanto Chemical Co., Inc.). It has been reported that lowering the Pt loading is preferable for quantitative adsorption of Ru(II) complex dyes onto the oxide surface.[34] Hence, this study adopted the same conditions based on that insight. It should be noted that TiO_2 (*X*) refers to photocatalysts prepared using JRC-TIO-*X* as the TiO_2 material, where *X* denotes the specific sample number. Likewise, TiO_2 (P25) and TiO_2 (Kanto)

refer to photocatalysts prepared from AEROXIDE TiO_2 P25 (NIPPON AEROSIL CO.) and anatase-type TiO_2 (Kanto Chemical Co., Inc.), respectively.

Preparation of RuP/Pt/TiO_2

$[Ru(4,4'\text{-}(CH_3)_2\text{-bpy})_2(4,4'\text{-}(PO_3H_2)_2\text{-bpy})]Cl_2$ (**RuP**, Chart 1a), synthesized according to a previous report,[35] was adsorbed by a stirring method onto Pt/TiO_2.[13] **RuP** aqueous solution (50 μM, 15 mL), adjusted to pH 4 with 2 M HCl, was added to a 200 mL Erlenmeyer flask containing Pt/TiO_2 powder (50 mg) and stirred for 15 h at room temperature in the dark. After stirring, the suspension was filtered using an Omnipore™ 0.1 μm PTFE membrane filter (47 mm, Merck Millipore), washed with water, and collected as a powder after drying at 343 K. The amount of adsorbed **RuP** on Pt/TiO_2 was estimated by using the following equation:

$$\text{Adsorbed amount } (\mu\text{mol g}^{-1}) = \frac{A_{\text{before}} - A_{\text{after}}}{A_{\text{before}}} \times \frac{C\ (\mu\text{mol L}^{-1}) \times V\ (\text{L})}{M\ (\text{g})}$$

where A_{before} and A_{after} indicate the absorbance of the **RuP** in a test solution at the singlet metal-to-ligand charge transfer (^{1}MLCT) maximum wavelength before and after the adsorption procedure, C is the concentration of the complex in the solution before adsorption, V is the volume of the **RuP**-containing solution, and M is the weight of the Pt/TiO_2 powder, respectively.

Preparation of [RuP, OPA]/Pt/TiO_2

RuP and octadecylphosphonic acid (**OPA**, see Chart 1b) (>98.0%, Tokyo Chemical Industry Co., Ltd) were co-adsorbed onto Pt/TiO_2 in a 1 : 1 molar ratio *via* a stirring method. A 50 μM solution of **RuP** and **OPA** was prepared in a mixed solvent consisting of *tert*-butyl alcohol (>99.0%, Tokyo Chemical Industry Co., Ltd) and acetonitrile (>99.5%, Kanto Chemical Co., Inc.)—each 7.5 mL, for a total volume of 15 mL. This solution was added to a 200 mL Erlenmeyer flask containing Pt/TiO_2 powder (50 mg), and the mixture was stirred at room temperature in the dark for 15 h. After stirring, the suspension was filtered using an Omnipore™ 0.1 μm PTFE membrane filter (47 mm, Merck Millipore), washed with water, and dried at 343 K to obtain the [**RuP**, **OPA**]/Pt/TiO_2 powder. The amount of **RuP** adsorbed was determined using the same method as for **RuP**/Pt/TiO_2.

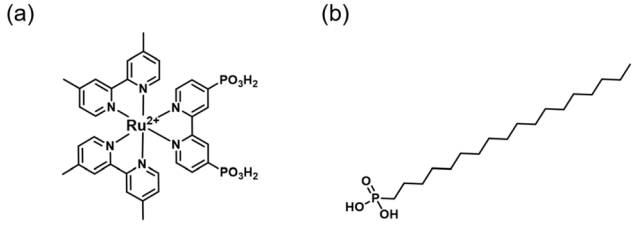

Chart 1 Molecular structures of (a) **RuP** and (b) **OPA**.

General characterization

X-ray diffraction (XRD) patterns were acquired using a powder X-ray diffractometer (Rigaku MiniFlex600) equipped with a Cu Kα radiation source operating at 40 kV and 15 mA. UV-visible diffuse reflectance spectra (DRS) and UV-visible absorption spectra were obtained using a spectrophotometer (V-770, JASCO), which has a spectral resolution of 0.1 nm. The measurements were conducted with a wavelength interval of 1.0 nm.

SSA was measured using a gas adsorption apparatus (MicrotracBEL, BELSORP-maxII) at liquid nitrogen temperature (77 K), and the data were analyzed by the BELMaster software and determined based on the Brunauer–Emmett–Teller theory. The Brunauer–Emmett–Teller equation was linearized as follows:

$$\frac{p}{v(p_0 - p)} = \frac{C - 1}{Cv_m} \times \frac{p}{p_0} + \frac{1}{Cv_m}$$

where v is the volume of gas adsorbed at a relative pressure (p/p_0), v_m is the monolayer adsorbed gas quantity, and C is the Brunauer–Emmett–Teller constant, respectively. The monolayer capacity (v_m) was determined from the linear region of the Brunauer–Emmett–Teller plot in the relative pressure range of $p/p_0 = 0.10$ to 0.25. The specific surface area (SSA) based on the Brunauer–Emmett–Teller theory was then calculated using the following equation:

$$\text{SSA} = \frac{v_m \times N_A \times \sigma}{V_m}$$

where N_A is Avogadro's number (6.022×10^{23} mol^{-1}), σ is the cross-sectional area of the adsorbate molecule (0.162 nm^2 for N_2), and V_m is the molar volume of gas at standard temperature and pressure (22.414 L mol^{-1}).

FT-IR spectra were measured using an FT/IR-4600 (JASCO) by the ATR method with a diamond prism. The instrument has a spectral resolution of 1.0 cm^{-1}, and the measurements were performed with a resolution setting of 4 cm^{-1} and a data interval of 1.0 cm^{-1}.

Photocatalytic reactions

The photocatalytic activity was primarily evaluated according to previously reported methods.[13] Photocatalyst powder (10 mg) was dispersed in 100 mL of a 10 mM EDTA·2Na (≥99.5%, Dojindo Laboratories) aqueous solution, which served as a sacrificial electron donor. The pH of the solution was adjusted to approximately 4 using H_2SO_4. After degassing the reaction cell, a small amount of Ar gas was introduced, and the mixture was irradiated for 3 h using a LED (Asahi Spectra Co., CL-1501, 450 nm) under 0.30 mW cm^{-2} (the irradiation area was 39 cm^2) in the wavelength range of 360–560 nm, as measured by using a calibrated silicon photodiode, in a closed gas circulation system to investigate H_2 evolution. The evolved gases were analyzed by gas chromatography (Shimadzu, GC-2014 with a TCD detector and an MS-5A column, Ar carrier gas).

The apparent quantum (AQY) for H_2 evolution was measured with $\lambda = 450$ nm and was estimated according to the following equation:

$$\text{AQY}\ (\%) = \frac{A \times R}{I} \times 100$$

where A, R, and I represent the reaction coefficient, the H_2 evolution rate, and the rate of incident photons, respectively. The AQY values are calculated with the assumption that one photoinjected electron can produce one H_2 molecule through current doubling, hence the assumption of $A = 1$.[36] The rate of incident photons was measured by using a calibrated silicon photodiode. The spectral irradiance is shown in Fig. S1.

Transient absorption spectroscopy

Transient absorption measurements for the assessment of back electron transfer (BET) rates were performed using an enVISion transient absorption spectroscopy system (Magnitude Instruments, State College, PA). The second harmonic of a Nd:YAG laser ($\lambda = 532$ nm) was used as the excitation source, while a xenon lamp was used as the probe light. The probe beam was dispersed through a monochromator and detected by a photodiode detector. The measurements were conducted with a temporal resolution of 1 ns per point. 10 mg **RuP**/Pt/TiO_2 samples were dispersed in either pure water or 10 mM EDTA aqueous solution, both adjusted to pH $\approx$ 4, and sealed in a quartz cuvette for measurement. The measurements were conducted in diffuse reflectance mode, and the suspension was purged with Ar for more than 20 min prior to the measurements. The transient absorption spectra were recorded to monitor the bleaching signal derived from the ^{1}MLCT absorption of **RuP** and its subsequent recovery over time. The decay of the oxidized **RuP** species was used to evaluate the rate of BET. The resulting temporal profiles were analyzed by exponential fitting to extract lifetime components. All the profiles could be fitted by a following triple-exponential function:

$$f(x) = y_0 - A_1 \exp\left(-\frac{x - x_0}{\tau_1}\right) - A_2 \exp\left(-\frac{x - x_0}{\tau_2}\right) - A_3 \exp\left(-\frac{x - x_0}{\tau_3}\right)$$

Time-correlated emission measurements

Emission lifetime measurements were performed using a lifetime spectrometer (HORIBA, DeltaFlex) equipped with a pulsed laser diode excitation source (HORIBA, DeltaDiode, 451 nm) and with emission monitored at 630 nm. The measurements were conducted with a bin width of 0.42 ns, which corresponds to the time resolution of the system. Samples were prepared by introducing 3 mg of **RuP**/Pt/TiO_2 and 4 mL of aqueous HCl solution (pH 4) into a dedicated measurement cell, followed by 30 minutes of Ar bubbling to remove dissolved gases. All the profiles could be fitted by a following triple-exponential function:

$$f(x) = y_0 + A_1 \exp\left(-\frac{x - x_0}{\tau_{e1}}\right) + A_2 \exp\left(-\frac{x - x_0}{\tau_{e2}}\right) + A_3 \exp\left(-\frac{x - x_0}{\tau_{e3}}\right)$$

Emission quantum yield measurements

Emission quantum yields were measured using a UV-NIR absolute PL quantum yield spectrometer (HAMAMATSU, Quantaurus-QY Plus) equipped with a 150 W xenon lamp, with excitation at 451 nm. The spectral resolution of the instrument is <2.5 nm. Measurements were carried out by introducing 3 mg of **RuP**/Pt/TiO_2 and 4 mL of aqueous HCl solution (pH 4) into a dedicated measurement cell, followed by 30 minutes of Ar bubbling to remove dissolved gases.

Steady-state emission measurements

Emission spectra were measured using a spectrofluorophotometer (Shimadzu, RF-6000) equipped with a 150 W xenon lamp, with excitation at 451 nm. The instrument's spectral resolution is ≤1.0 nm (emission bandwidth), and the spectra were recorded with a wavelength interval of 1.0 nm. Measurements were conducted after introducing 3 mg of **RuP**/Pt/TiO_2 and 4 mL of aqueous HCl solution (pH 4) into a dedicated measurement cell, followed by 30 minutes of Ar bubbling to remove dissolved gases.

Results and discussion

Preparation of RuP-adsorbed Pt/TiO_2

UV-vis diffuse reflectance spectra (DRS) were measured for TiO_2, Pt/TiO_2, and **RuP**/Pt/TiO_2 samples. As displayed in Fig. 1a, a characteristic background rise in the visible region was observed upon Pt loading, indicating the successful deposition of Pt nanoparticles. Given the same Pt loading of 0.10 wt%, the particle size of Pt nanoparticles is generally reported to be around 2–4 nm.[34] Additionally, an absorption band attributed to the ^{1}MLCT transition of **RuP** was detected, confirming that **RuP** was adsorbed onto the surface of TiO_2.

Furthermore, the adsorption amount of **RuP** was quantified by comparing the absorption spectra of the **RuP** aqueous solution before and after adsorption. The absorbance at around 460 nm was measured for the initial 50 μM **RuP** solution and the filtrate obtained after adsorption (Fig. 1b), and the adsorbed amount was calculated based on the difference. As a result, most TiO_2 samples, including the JRC-TIO series, achieved quantitative adsorption of **RuP**, with an adsorbed amount of 15

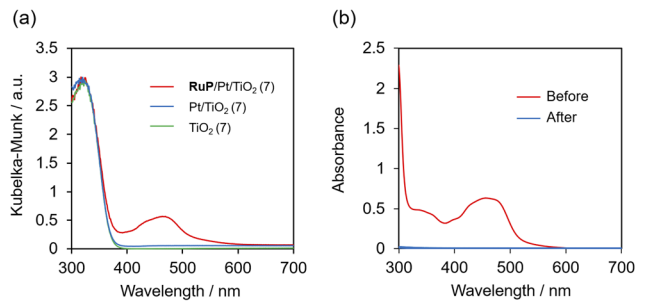

Fig. 1 (a) UV-vis DRS of **RuP**/Pt/TiO_2, Pt/TiO_2 and TiO_2 (7), (b) UV-vis absorption spectra of **RuP** aqueous solution (50 μM) (red line) and the filtrate after adsorption onto Pt/TiO_2 (7) (blue line).

μmol g^{-1}. On the other hand, the anatase-type TiO_2 from Kanto Chemical exhibited a slightly lower value of 12.3 μmol g^{-1}.

Determination of specific surface area and surface coverage

The specific surface areas (SSAs) of the various TiO_2 samples were measured by the Brunauer–Emmett–Teller method. The full adsorption/desorption isotherms data are provided in Fig. S2. As listed in Table 1, anatase-type TiO_2 such as TiO_2 (7) and TiO_2 (10) exhibited high SSAs of 250–300 m^2 g^{-1}, whereas samples like TiO_2 (13) and TiO_2 (Kanto) showed lower values, below 50 m^2 g^{-1}.

Despite similar amounts of adsorbed **RuP**, the difference in SSAs led to variations in surface coverage. The fractional coverage was calculated by assuming a molecular diameter of 12.3 Å for **RuP**.[13] It was found that TiO_2 samples with high surface areas had a dye coverage lower than 5%, whereas for low surface area TiO_2 samples, the coverage could exceed 20%.

Photocatalytic activity

H_2 evolution experiments using **RuP**/Pt/TiO_2 were conducted to evaluate the photocatalytic activity of various TiO_2 samples. The H_2 evolution AQYs were summarized in Table 1, and the corresponding time course data are shown in Fig. 2. Regarding the influence of crystal structure, the observed trend in activity was anatase ≥ P25 (anatase/rutile mixed phase) > rutile. The influence of specific surface area was particularly evident among anatase-type samples (Fig. 3); those with larger specific surface areas, such as TiO_2 (7) and TiO_2 (10), exhibited significantly higher H_2 evolution activity compared to samples with smaller specific surface areas, such as TiO_2 (13) and TiO_2 (Kanto). In this study, the loading amount of Pt and the adsorption amount of **RuP** were unified for all samples except for TiO_2 (Kanto), thereby eliminating variations due to differences in the number of active sites or dye loading. Therefore, the observed differences in photocatalytic activity can be attributed to intrinsic differences in crystal structure and specific surface area.

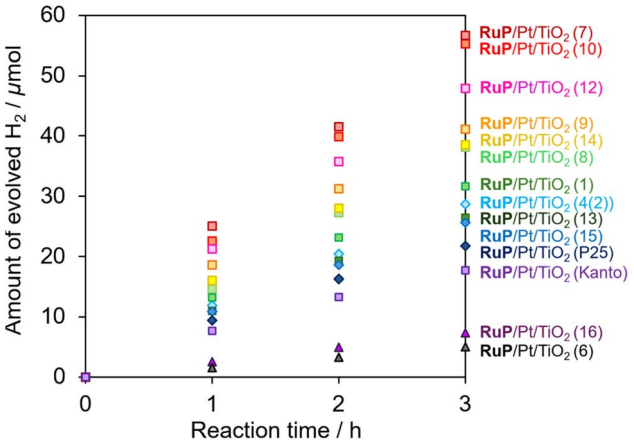

Fig. 2 Time courses of H_2 evolution of **RuP**/Pt/TiO_2. Reaction conditions: catalyst, 10 mg; solution, aqueous EDTA solution (10 mM, 100 mL, pH 4); light source, LED (Asahi Spectra Co., CL-1501, 450 nm) under 0.30 mW cm^{-2} (the irradiation area is 39 cm^2). Symbols: □, anatase; ◇, P25; △, rutile. Numbers in parentheses correspond to sample designations in Table 1.

XRD measurement for the most active TiO_2 (7) sample showed that the crystal structure of TiO_2 remained unchanged after the reaction (Fig. S3a). While the overall spectral shape of UV-vis absorption spectra was retained, a slight red-shift was observed after the reaction (Fig. S3b). This shift suggests that the **RuP** dye may have undergone partial degradation,[13,37] which could explain the deactivation of H_2 evolution rate over time (Fig. 2).

Table 1 Specific surface areas (SSAs) of TiO_2, adsorption amount of **RuP** on Pt/TiO_2, coverage of **RuP** and H_2 evolution AQY of **RuP**/Pt/TiO_2

TiO_2	SSA/m^2 g^{-1}	Crystal structure[a]	Adsorbed **RuP**/μmol g^{-1}	Coverage[b]/%	AQY/%
TiO_2 (1)	76.2	A	15	14.1	6.7
TiO_2 (4(2))	53.9	A/R	15	20.0	6.0
TiO_2 (6)	85.2	R	15	12.6	1.1
TiO_2 (7)	268	A	15	4.0	12.0
			12	3.2	10.4
			9	2.4	5.2
TiO_2 (8)	252	A	15	4.3	8.0
			12	3.4	7.3
			9	2.6	6.1
TiO_2 (9)	230	A	15	4.7	8.7
TiO_2 (10)	290	A	15	3.7	11.7
TiO_2 (12)	303	A	15	3.5	10.2
TiO_2 (13)	48.6	A	15	22.1	5.6
			12	17.7	7.4
			9	13.2	6.5
TiO_2 (14)	276	A	15	3.9	8.2
TiO_2 (15)	52.4	A/R	15	20.5	5.4
TiO_2 (16)	97.9	R	15	11.0	1.5
TiO_2 (Kanto)	22.6	A	12.3	39.1	3.8
TiO_2 (P25)	53.8	A/R	15	20.0	4.6

[a] A: anatase, R: rutile. [b] According to the previous report,[13] the diameter of **RuP** was assumed to be 12.3 Å for the calculation.

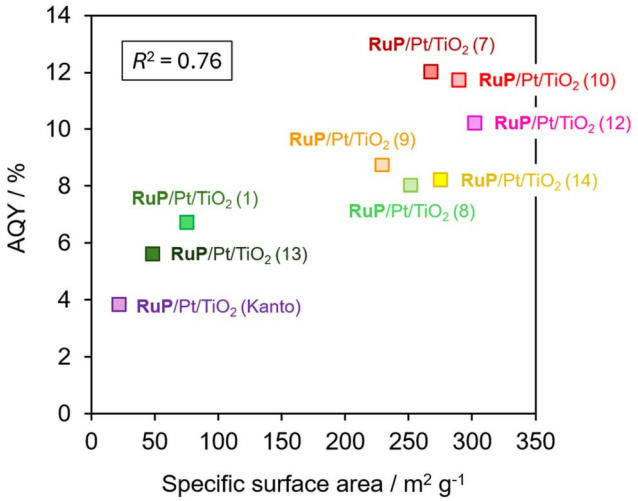

Fig. 3 The relationship between specific surface area of TiO_2 and H_2 evolution AQY. Only anatase-containing samples are shown. The correlation coefficient (R^2) between AQY and specific surface area was calculated to be 0.76.

Evaluation of the electron injection process by emission lifetime measurements

The result of photocatalytic reactions indicated that when using samples with specific surface areas of 50–100 $m^2\ g^{-1}$, the trend in activity followed the order of anatase ≈ P25 > rutile under identical reaction conditions. This result is consistent with previously reported findings in dye-sensitized solar cells, where rutile exhibits lower photoelectrochemical conversion efficiency than anatase or P25, primarily due to its lower specific surface area and reduced dye adsorption.[22,30] However, since dye loading was standardized in the present study, the difference in photocatalytic activity cannot be attributed to variations in dye adsorption.

To evaluate the electron injection process from the excited state of **RuP** into TiO_2, emission lifetime measurements were conducted using several selected TiO_2 samples. For comparison, the excited state decay rate of **RuP** adsorbed on the insulating material Al_2O_3 was also measured. Since Al_2O_3 is an insulator, electron injection from the excited state of **RuP** into Al_2O_3 does not occur.[13] Additionally, the emission quantum yield of **RuP**/Al_2O_3 was 4.5%, which is generally consistent with previously reported values for **RuP** adsorbed on Al_2O_3.[13]

The emission decay of **RuP**/Pt/TiO_2 was clearly faster than that of **RuP**/Al_2O_3, indicating efficient electron injection into TiO_2 (Fig. 4 and Table 2). Although the emission lifetime of **RuP**/Pt/TiO_2 was different from sample to sample, no clear correlation with photocatalytic activity was found. The emission quantum yields of all samples were below 1%, suggesting that electron injection from the excited state of **RuP** proceeds with high efficiency. Previous studies have pointed out that when emission quenching is on the order of several tens of percent, electron injection efficiency may influence photocatalytic activity.[36] Since more than 90% quenching was observed in this study, it is unlikely that electron injection is the dominant factor governing photocatalytic activity.

Nevertheless, variations in emission lifetimes provide useful insight into interfacial electron transfer behavior. A comparison of **RuP**/Pt/TiO_2 systems employing anatase-, rutile-, and mixed-phase TiO_2 revealed that the sample using rutile-type TiO_2 clearly exhibited a shorter emission lifetime than the others (Fig. 4 and Table 2). Specifically, anatase-type TiO_2 exhibited predominantly long-lived components with lifetimes on the order of several hundred nanoseconds, whereas rutile-type TiO_2 was characterized by extremely short-lived components with lifetimes of 2 ns or less. This difference in emission lifetimes is considered to arise from differences in surface structure and the distribution of trap states between the two materials.

Anatase-type TiO_2 has a large specific surface area but low crystallinity and small particle size, which suggests the presence of numerous surface defects and heterogeneous crystal facets. These features are thought to lead to inhomogeneous adsorption modes of **RuP**, resulting in diverse interfacial environments with varying electron injection efficiencies. Since the emission quantum yield of **RuP**/Pt/TiO_2 was below 1%, it is inferred that the majority of excited **RuP** molecules were deactivated through electron injection or nonradiative processes. On the other hand,

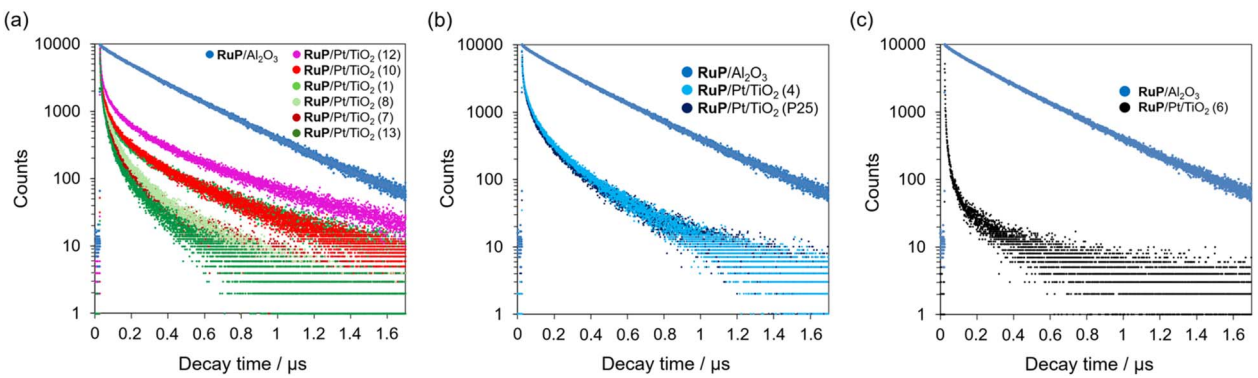

Fig. 4 Emission lifetimes of **RuP**/Pt/TiO_2 samples with different TiO_2 crystal structures: (a) anatase, (b) mixed phase of anatase and rutile, and (c) rutile. Emission lifetime measurements were performed after introducing 4 mL of an aqueous HCl solution (pH 4) and 3 mg of **RuP**/Pt/TiO_2 into a dedicated cell, followed by 30 minutes of Ar bubbling to remove dissolved gases, using an excitation wavelength of 451 nm and monitoring the emission at 630 nm.

Table 2 Emission lifetimes and emission quantum yields of **RuP**/Pt/TiO_2[a]

Sample[b]	Crystal structure[c]	Emission lifetimes/ns			Φ_{em}/%
		τ_{e1} (%)	τ_{e2} (%)	τ_{e3} (%)	
Al_2O_3	—	50 ± 8 (2)	301 ± 2.2 (98)	—	4.5
TiO_2 (12)	A	3.9 ± 0.2 (5)	33 ± 2 (22)	226 ± 5.3 (73)	1.0
TiO_2 (10)	A	3.0 ± 0.2 (8)	26 ± 2 (29)	174 ± 5.0 (63)	0.5
TiO_2 (1)	A	3.5 ± 0.2 (10)	26 ± 2 (28)	186 ± 6.0 (62)	0.5
TiO_2 (8)	A	4.0 ± 0.2 (12)	28 ± 2 (41)	130 ± 4.0 (47)	0.5
TiO_2 (7)	A	3.4 ± 0.2 (14)	24 ± 2 (42)	128 ± 4.0 (44)	0.3
TiO_2 (13)	A	4.2 ± 0.2 (18)	25 ± 2 (46)	138 ± 4.6 (36)	0.5
TiO_2 (4)	A/R	2.9 ± 0.2 (6)	28 ± 2 (28)	150 ± 3.3 (63)	0.8
TiO_2 (P25)	A/R	3.9 ± 0.3 (7)	28 ± 2 (31)	152 ± 3.6 (62)	0.5
TiO_2 (6)	R	0.23 ± 0.07 (27)	1.9 ± 0.4 (54)	85 ± 30 (19)	0.1

[a] The emission lifetimes were calculated from the emission decay curves shown in Fig. 4. [b] **RuP** (15 μmol g^{-1}) was adsorbed. For TiO_2, 0.10 wt% Pt was loaded. [c] A: anatase, R: rutile.

the small amount of detectable emission is considered to originate from **RuP** molecules adsorbed at sites where electron injection is less favorable, leading to relatively long-lived emission.

This relationship among the uniformity of the TiO_2 surface, the adsorption state of **RuP**, and the resulting emission behavior is also reflected the emission spectra. In particular, notable differences in emission peak wavelengths were observed even among samples employing the same anatase-type TiO_2. As shown in Fig. 5, distinct variations in peak positions were found across samples, suggesting differences in the molecular conformation or orientation of **RuP** at the TiO_2 interface. For instance, the spectra of **RuP**/Pt/TiO_2 (1), (10), and (12) exhibited emission peaks around 630 nm, resembling that of $Ru(bpy)_3^{2+}$ in solution,[38] implying that **RuP** may be adsorbed in a conformation similar to that in solution. In contrast, samples such as **RuP**/Pt/TiO_2 (13) showed peaks around 670 nm, suggesting that **RuP** molecules are predominantly adsorbed in different adsorption states on the TiO_2 surface. Given that the samples showing peaks around 630 nm tended to exhibit relatively long emission lifetimes, it is likely that **RuP** is more weakly adsorbed onto the TiO_2 surface in these cases, resulting in weaker electronic coupling and suppressed electron injection.

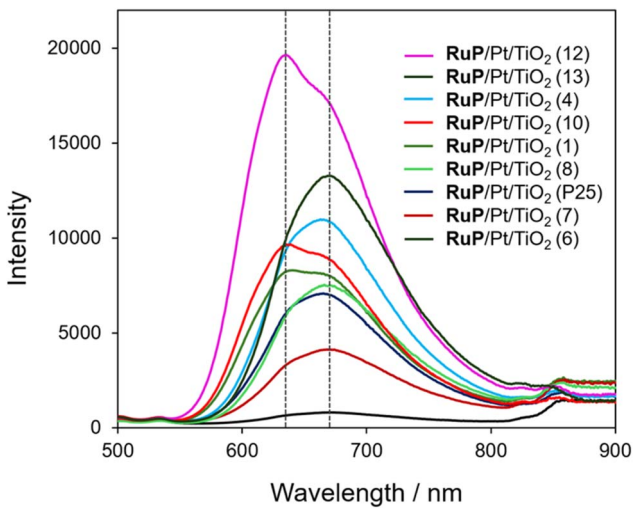

Fig. 5 Emission spectra of **RuP**/Pt/TiO_2. Samples were prepared by introducing 3 mg of **RuP**/Pt/TiO_2 and 4 mL of aqueous HCl solution (pH 4) into a dedicated measurement cell, followed by 30 minutes of Ar bubbling to remove dissolved gases, using an excitation wavelength of 451 nm.

In contrast, rutile-type TiO_2 is known to possess deep trap states, which are primarily associated with surface defects.[28,39] Given that **RuP** molecules are adsorbed directly on the TiO_2 surface, it is highly plausible that electron injection from the excited state of **RuP** occurs directly into these surface-localized trap states. Furthermore, the larger energy offset (*i.e.*, greater driving force) between the excited state oxidation potential of **RuP** and the trap states in rutile compared to anatase may facilitate a faster electron injection process. Consequently, the fraction of **RuP** contributing to emission is significantly reduced, and the observed photoluminescence likely arises only on a very short timescale, in direct competition with ultrafast electron injection.

Effect of crystal structure on back electron transfer

To elucidate the origin of the activity differences associated with crystal structure, transient absorption spectroscopy was employed to measure the rate of BET from the semiconductor to the oxidized state of **RuP**. Measurements were carried out in the absence of an electron donor, such that the recovery of the bleaching signal reflects the BET process.

As shown in Fig. 6a, the results revealed that the BET rates for anatase and P25 were comparable, whereas the decay of the oxidized **RuP** species was significantly faster for rutile, indicating an accelerated BET process. To further interpret these results, the bleaching recovery curves were fitted with a triple-exponential function, yielding three lifetime components (τ_1–τ_3) (Table 3). These components are arranged in order of increasing lifetime and do not necessarily correspond to

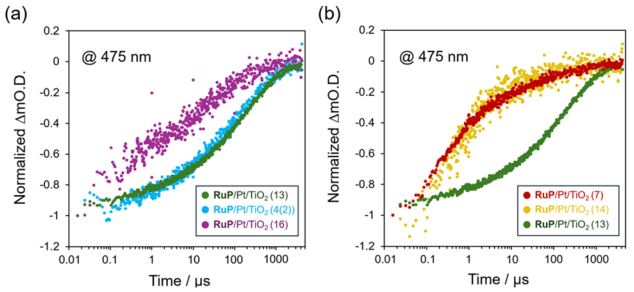

Fig. 6 Normalized ΔAbsorbance at 475 nm of **RuP**/Pt/TiO_2 as a function of time. (a) Comparison of samples with anatase and rutile TiO_2 crystal structures. (b) Comparison with anatase-type TiO_2 samples having different specific surface areas. Experimental conditions: water (adjusted to pH ≈ 4 by addition of sulfuric acid); excitation wavelength, 532 nm.

discrete elementary processes. However, based on the classification proposed by Nishioka *et al.*,[18] they can be tentatively assigned according to their timescales as follows: components shorter than 10 μs are associated with radiative or nonradiative deactivation of excited **RuP** that did not undergo electron injection, or with ultrafast BET from the conduction band to the oxidized **RuP**; components in the range of 10–100 μs are attributed to BET from relatively deep trap states; and components longer than 100 μs reflect slow BET processes involving spatially separated charge carriers. The faster decay of the oxidized **RuP** species observed for the rutile sample, corresponding to shorter BET-related lifetimes, correlates well with the lower photocatalytic activity of this sample, suggesting that the lower performance of rutile-type TiO_2 is likely associated with its accelerated BET.

This interpretation is also consistent with the emission lifetime measurements. In the rutile sample, a significantly faster emission decay was observed compared to anatase, suggesting that a considerable fraction of electrons from excited **RuP** are directly injected into deep trap states located on the TiO_2 surface. Electrons trapped in such states lose their mobility, and if oxidized **RuP** species are present nearby, BET can proceed rapidly. Since this process is strongly favorable energetically, it is expected to occur very efficiently. Furthermore, electrons injected into deep trap states cannot participate in the H_2 evolution reaction in the same way as free electrons in the conduction band, which likely contributes to the lower photocatalytic activity observed in rutile-based systems.

Even under conditions where an electron donor (EDTA) was added, transient absorption measurements showed that the trend of accelerated BET to the oxidized **RuP** species in the rutile sample remained unchanged (Fig. S4). Nonetheless, since the rutile sample possessed a slightly larger specific surface area than the other samples, the possibility that this contributed in part to the observed activity differences cannot be completely excluded. As the conduction band minimum of rutile TiO_2 is more positive than that of anatase, the driving force for H_2 evolution by the conduction band electron is smaller in rutile than in anatase.[40] This could be a contributor to the low H_2 evolution activity of the rutile-based systems.

Effect of specific surface area on back electron transfer

The influence of specific surface area on BET was also examined in a similar manner. Fig. 6b showed that among anatase-type TiO_2 samples, the oxidized **RuP** species exhibited a longer lifetime on samples with smaller specific surface area (*e.g.*, TiO_2 (13)), and a shorter lifetime on those with larger specific surface area (*e.g.*, TiO_2 (7)). At first glance, this result appears inconsistent with the experimental finding that samples with higher specific surface area showed higher photocatalytic activity. One possible explanation for this discrepancy could be that TiO_2 with larger specific surface areas tend to have smaller particle sizes, which might shift the conduction band edge to more negative potentials due to quantum size effects.[41] This shift could enhance the driving force for the H_2 evolution reaction, thereby leading to higher H_2 production in samples with larger specific surface areas. However, although a slight blue shift was observed in the absorption edge of some samples, DRS measurements showed only minimal spectral changes across the TiO_2 series (Fig. S5). This suggests that the contribution of quantum size effects to the increase in the bandgap—and hence to the enhancement of the driving force for H_2 evolution—is likely to be minor in this case.

Instead, the observed discrepancy is more likely attributable to differences in the crystallinity of TiO_2. Highly crystalline TiO_2 generally contains fewer defect-related trap sites, allowing injected electrons to diffuse over longer distances before recombination. This extended electron transport can prolong the lifetime of the oxidized **RuP** species and suppress BET.

Table 3 Absorption decay lifetimes of **RuP**/Pt/TiO_2[a]

		Lifetimes/μs		
Sample[b]	Crystal structure[c]	τ_1 (%)	τ_2 (%)	τ_3 (%)
TiO_2 (16)	R	0.30 ± 0.07 (10)	12 ± 3 (47)	200 ± 50 (43)
TiO_2 (4(2))	A/R	2.1 ± 0.5 (11)	38 ± 7 (39)	440 ± 60 (50)
TiO_2 (13)	A	2.3 ± 0.4 (20)	48 ± 6 (33)	500 ± 40 (47)
TiO_2 (7)	A	0.34 ± 0.03 (34)	4.0 ± 0.6 (38)	115 ± 18 (28)
TiO_2 (14)	A	0.23 ± 0.07 (27)	1.9 ± 0.4 (54)	85 ± 30 (19)

[a] Calculated from the bleaching recovery curves shown in Fig. 6. [b] **RuP** (15 μmol g^{-1}) was adsorbed. For TiO_2, 0.10 wt% Pt was loaded. [c] A: anatase, R: rutile.

Indeed, previous studies comparing materials with different crystallinities have shown that higher crystallinity leads to more efficient electron transfer and reduced BET *via* defect states.[19] A similar mechanism is likely operative in the present system, where the slower BET can be attributed to improved charge transport associated with higher crystallinity. In addition, for samples with higher specific surface area, the longest BET component (sub-100 μs) was not observed, which may be due to their smaller particle sizes limiting the spatial separation of charge carriers. These findings suggest that the differences in photocatalytic activity arising from specific surface area are primarily influenced by factors other than BET.

Effect of intermolecular interactions among RuP molecules

Based on the above results, we hypothesized that the specific surface area-dependent variation in activity could be influenced by the intermolecular distance between **RuP** molecules on the TiO_2 surface. Since dye loading was kept constant across samples, those with smaller specific surface area are expected to have shorter intermolecular distances between dye molecules than those with larger specific surface area. Consequently, intermolecular interactions may become non-negligible and potentially lead to lower photocatalytic activity.

To test this hypothesis, **RuP**/Pt/TiO_2 samples were prepared with intentionally reduced dye loadings (12 and 9 μmol g^{-1}), and their photocatalytic activities were compared. In the case of TiO_2 (7) and TiO_2 (8) with high specific surface area, reducing the **RuP** loading resulted in decreased H_2 evolution activity, as expected (Fig. 7). However, in the case of TiO_2 (13) with low specific surface area, a counterintuitive increase in H_2 production was observed. While lower dye loading typically limits light absorption and lowers activity, the enhancement observed for the low specific surface area sample supports the notion that intermolecular interactions among **RuP** molecules negatively affect photocatalytic performance.

To further investigate whether these interactions involve dye aggregation, octadecylphosphonic acid (**OPA**), a co-adsorbent known to suppress aggregation,[42] was used to prepare [**RuP**, **OPA**]/Pt/TiO_2 samples. FT-IR measurements were conducted to confirm the co-adsorption of **OPA**. In both the **OPA**-only sample and the [**RuP**, **OPA**]/Pt/TiO_2 sample, absorption bands were observed near 2900 cm^{-1}, corresponding to C–H stretching vibrations from the alkyl chains, indicating that **OPA** was successfully adsorbed onto the TiO_2 surface (Fig. 8). As shown in Fig. 9, the co-adsorption of **OPA** improved H_2 evolution for samples based on low specific surface area TiO_2 (13). In contrast, no significant effect was observed for higher specific surface area TiO_2 (10). These findings provide the evidence that intermolecular interactions among **RuP** molecules play a critical role in determining photocatalytic activity, particularly for TiO_2 with low specific surface area.

To gain further insight into the nature of these intermolecular interactions, we analyzed both the absorption spectra and the emission lifetimes—parameters commonly used to assess dye aggregation (Fig. S6–S8). While the absorption spectra showed no significant differences upon co-adsorption of **OPA**, a clear increase in emission lifetime was observed. This result suggests that non-radiative deactivation pathways, likely caused by dye–dye interactions, were suppressed in the presence of **OPA**. Such behavior is consistent with previous reports attributing shortened emission lifetimes to dye aggregation. For example, it has been reported that $[Ru(bpy)_3]^{2+}$ adsorbed into mesoporous silica exhibits significant luminescence quenching upon dehydration due to aggregation of the dye molecules.[43] It has been also reported that in dye-sensitized photoelectrochemical cells for water splitting, dye aggregation could enhance the rate of hole transfer between dye molecules, thereby promoting hole transport to an O_2 evolution catalyst such as IrO_x.[44] In contrast, in the present **RuP**/Pt/TiO_2 system, electrons injected from the excited state of **RuP** into TiO_2 may be scavenged by holes migrating between adjacent **RuP** molecules (*i.e.*, BET reaction may occur) before reaching the Pt cocatalyst where H_2 evolution occurs. The introduction of **OPA** between dye molecules may serve to inhibit this inter-dye hole transport pathway, thereby suppressing undesirable charge recombination. Therefore, it is highly probable that intermolecular interactions, including aggregation, are operative in our system and contribute to variations in photocatalytic activity.

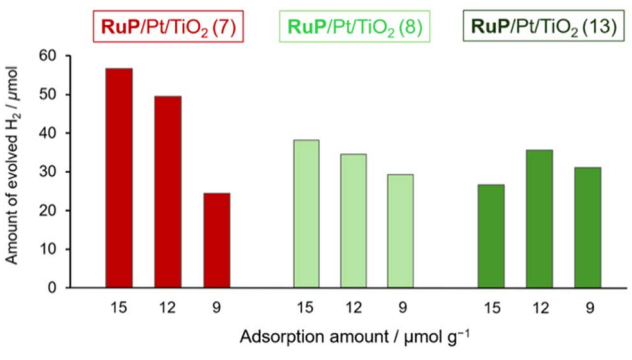

Fig. 7 Effect of lowering the dye loading on H_2 production by **RuP**/Pt/TiO_2 after 3 hours of irradiation. Reaction conditions: catalyst, 10 mg; solution, aqueous EDTA solution (10 mM, 100 mL, pH 4); light source, LED (Asahi Spectra Co., CL-1501, 450 nm) under 0.30 mW cm^{-2} (the irradiation area is 39 cm^2).

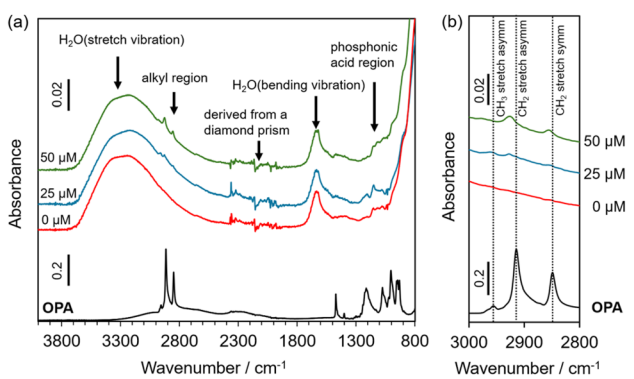

Fig. 8 FT-IR spectra of **RuP**/Pt/TiO_2 (8) adsorbed with **OPA**; from bottom to top: **OPA** only, **RuP**/Pt/TiO_2, [**RuP**, **OPA**]/Pt/TiO_2 (**RuP** : **OPA** = 1 : 0.5, **OPA**: 25 μM), [**RuP**, **OPA**]/Pt/TiO_2 (**RuP** : **OPA** = 1 : 1, **OPA**: 50 μM). (a) Overview, (b) enlarged view for alkyl region.

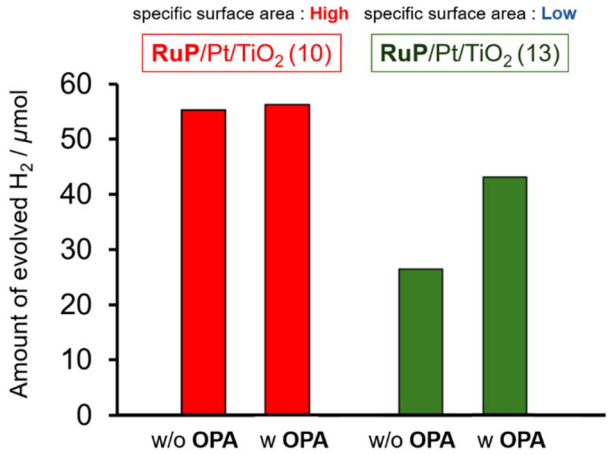

Fig. 9 Comparison of H_2 production by **RuP**/Pt/TiO_2 and [**RuP**, OPA]/Pt/TiO_2 using TiO_2 with different specific surface areas after 3 hours of irradiation. Reaction conditions: catalyst, 10 mg; solution, aqueous EDTA solution (10 mM, 100 mL, pH 4); light source, LED (Asahi Spectra Co., CL-1501, 450 nm) under 0.30 mW cm^{-2} (the irradiation area is 39 cm^2).

Taken together, the observed specific surface area-dependent differences in photocatalytic activity for dye-sensitized TiO_2 systems could be explained by the interplay between BET and intermolecular interactions among dye molecules. In this system, the negative impact of dye–dye interactions appears to play a more dominant role than the losses due to BET in determining overall photocatalytic performance.

Conclusions

In this study, the effects of TiO_2 crystal structure and specific surface area on the photocatalytic activity of **RuP**/Pt/TiO_2 systems were systematically investigated through H_2 evolution experiments. The results showed that differences in activity due to crystal structure were primarily attributed to variations in BET rates, with rutile-type TiO_2 exhibiting significantly lower performance owing to its faster BET. In contrast, the influence of specific surface area could not be fully explained by BET rates alone; in particular, for anatase-type samples with low specific surface area, intermolecular interactions among **RuP** molecules were suggested to be a major factor limiting activity.

Based on these findings, the design of high-efficiency photocatalysts should involve the selection of crystal structures that suppress BET, while also incorporating strategies to minimize intermolecular interactions among dye molecules. Specifically, employing semiconductors with large specific surface areas or applying techniques—such as the use of co-adsorbents—to inhibit dye–dye interactions may prove effective.

Author contributions

K. M. and T. E. M. designed/supervised the project and wrote the manuscript draft with K. H. K. H. conducted catalyst preparation, photocatalytic reactions, and main characterization with H. Y. and M. O. All authors reviewed the manuscript and approved its submission. The authors thank Prof. Mio Kondo and Mr Kazuki Kyuma (Institute of Science Tokyo) for assistance in emission and XRD measurements, respectively.

Conflicts of interest

There are no conflicts to declare.

Data availability

The data supporting this article have been included as part of the SI. See DOI: https://doi.org/10.1039/d5ta05528h.

Acknowledgements

This work was supported by JSPS-KAKENHI (JP22H01862, JP22H05142, JP22H05148, JPJSCCA20200004). Research at the University of Pennsylvania was supported by the Office of Basic Energy Sciences, Division of Chemical Sciences, Geosciences, and Energy Biosciences, Department of Energy, under Contract DE-SC0019781.

Notes and references

1 A. Kudo and Y. Miseki, *Chem. Soc. Rev.*, 2009, **38**, 253–278.
2 S. Nishioka, F. E. Osterloh, X. Wang, T. E. Mallouk and K. Maeda, *Nat. Rev. Methods Primers*, 2023, **3**, 42.
3 K. Maeda and K. Domen, *Bull. Chem. Soc. Jpn.*, 2016, **89**, 627–648.
4 J. Cui, C. Li and F. Zhang, *ChemSusChem*, 2019, **12**, 1872–1888.
5 A. Miyoshi and K. Maeda, *Sol. RRL*, 2021, **5**, 2000521.
6 D. Kato, H. Suzuki, R. Abe and H. Kageyama, *Chem. Sci.*, 2024, **15**, 11719–11736.
7 Y. Sakata, T. Hayashi, R. Yasunaga, N. Yanaga and H. Imamura, *Chem. Commun.*, 2015, **51**, 12935–12938.
8 T. Takata, J. Jiang, Y. Sakata, M. Nakabayashi, N. Shibata, V. Nandal, K. Seki, T. Hisatomi and K. Domen, *Nature*, 2020, **581**, 411–414.
9 W. J. Youngblood, S.-H. A. Lee, K. Maeda and T. E. Mallouk, *Acc. Chem. Res.*, 2009, **42**, 1966–1973.
10 M. Watanabe, *Sci. Technol. Adv. Mater.*, 2017, **18**, 705–723.
11 R. Abe, K. Shinmei, K. Hara and B. Ohtani, *Chem. Commun.*, 2009, 3577–3579.
12 R. Abe, K. Shinmei, N. Koumura, K. Hara and B. Ohtani, *J. Am. Chem. Soc.*, 2013, **135**, 16872–16884.
13 T. Oshima, S. Nishioka, Y. Kikuchi, S. Hirai, K. I. Yanagisawa, M. Eguchi, Y. Miseki, T. Yokoi, T. Yui, K. Kimoto, K. Sayama, O. Ishitani, T. E. Mallouk and K. Maeda, *J. Am. Chem. Soc.*, 2020, **142**, 8412–8420.
14 S. Nishioka, K. Hojo, L. Xiao, T. Gao, Y. Miseki, S. Yasuda, T. Yokoi, K. Sayama, T. E. Mallouk and K. Maeda, *Sci. Adv.*, 2022, **8**, eadc9115.
15 H. Yamamoto, S. Nishioka, L. Xiao, Y. Miseki, K. Sayama, T. E. Mallouk and K. Maeda, *Sol. RRL*, 2023, **7**, 2300629.

16 H. Yamamoto, L. Xiao, Y. Miseki, H. Ueki, M. Okazaki, K. Sayama, T. E. Mallouk and K. Maeda, *Chin. J. Catal.*, 2024, **63**, 124–132.
17 W. Kim, T. Tachikawa, T. Majima and W. Choi, *J. Phys. Chem. C*, 2009, **113**, 10603–10609.
18 S. Nishioka, T. Oshima, S. Hirai, D. Saito, K. Hojo, T. E. Mallouk and K. Maeda, *ACS Catal.*, 2021, **11**, 659–669.
19 K. Hojo, S. Nishioka, Y. Miseki, Y. Kamakura, T. Oshima, K. Sayama, T. E. Mallouk and K. Maeda, *ACS Appl. Energy Mater.*, 2021, **4**, 10145–10152.
20 Y. Tachibana, I. V. Rubtsov, I. Montanari, K. Yoshihara, D. R. Klug and J. R. Durrant, *J. Photochem. Photobiol., A*, 2001, **142**, 215–220.
21 S. A. Haque, Y. Tachibana, R. L. Willis, J. E. Moser, M. Grätzel, D. R. Klug and J. R. Durrant, *J. Phys. Chem. B*, 1999, **104**, 538–547.
22 N. G. Park, J. van de Lagemaat and A. J. Frank, *J. Phys. Chem. B*, 2000, **104**, 8989–8994.
23 F. Fabregat-Santiago, J. García-Cañadas, E. Palomares, J. N. Clifford, S. A. Haque, J. R. Durrant, G. Garcia-Belmonte and J. Bisquert, *J. Appl. Phys.*, 2004, **96**, 6903–6907.
24 Z.-S. Wang and G. Zhou, *J. Phys. Chem. C*, 2009, **113**, 15417–15421.
25 A. Hagfeldt, G. Boschloo, L. Sun, L. Kloo and H. Pettersson, *Chem. Rev.*, 2010, **110**, 6595–6663.
26 M. K. Brennaman, A. O. Patrocinio, W. Song, J. W. Jurss, J. J. Concepcion, P. G. Hoertz, M. C. Traub, N. Y. Iha and T. J. Meyer, *ChemSusChem*, 2011, **4**, 216–227.
27 J. W. Ondersma and T. W. Hamann, *J. Am. Chem. Soc.*, 2011, **133**, 8264–8271.
28 Y. Wang, D. Wu, L. M. Fu, X. C. Ai, D. Xu and J. P. Zhang, *ChemPhysChem*, 2015, **16**, 2253–2259.
29 V. S. Manthou, E. K. Pefkianakis, P. Falaras and G. C. Vougioukalakis, *ChemSusChem*, 2015, **8**, 588–599.
30 K. Al-Attafi, A. Nattestad, Q. Wu, Y. Ide, Y. Yamauchi, S. X. Dou and J. H. Kim, *Chem. Commun.*, 2018, **54**, 381–384.
31 S. Ikeda, C. Abe, T. Torimoto and B. Ohtani, *J. Photochem. Photobiol., A*, 2003, **160**, 61–67.
32 E. Bae and W. Choi, *J. Phys. Chem. B*, 2006, **110**, 14792–14799.
33 B. Kraeutler and A. J. Bard, *J. Am. Chem. Soc.*, 1978, **100**, 4317–4318.
34 S. Nishioka, K. Hojo, D. Saito, I. Yamamoto, T. E. Mallouk and K. Maeda, *Appl. Catal., A*, 2023, **654**, 119086.
35 D. L. Ashford, M. K. Brennaman, R. J. Brown, S. Keinan, J. J. Concepcion, J. M. Papanikolas, J. L. Templeton and T. J. Meyer, *Inorg. Chem.*, 2015, **54**, 460–469.
36 K. Maeda, M. Eguchi, S.-H. A. Lee, W. J. Youngblood, H. Hata and T. E. Mallouk, *J. Phys. Chem. C*, 2009, **113**, 7962–7969.
37 A. Nakada, K. Koike, T. Nakashima, T. Morimoto and O. Ishitani, *Inorg. Chem.*, 2015, **54**, 1800–1807.
38 D. W. Thompson, A. Ito and T. J. Meyer, *Pure Appl. Chem.*, 2013, **85**, 1257–1305.
39 A. Yamakata, J. J. M. Vequizo and H. Matsunaga, *J. Phys. Chem. C*, 2015, **119**, 24538–24545.
40 A. Miyoshi, S. Nishioka and K. Maeda, *Chem.–Eur. J.*, 2018, **24**, 18204–18219.
41 N. Satoh, T. Nakashima, K. Kamikura and K. Yamamoto, *Nat. Nanotechnol.*, 2008, **3**, 106–111.
42 Y. Liu, J. R. Jennings, X. Wang and Q. Wang, *Phys. Chem. Chem. Phys.*, 2013, **15**, 6170–6174.
43 M. Ogawa, T. Nakamura, J.-i. Mori and K. Kuroda, *J. Phys. Chem. B*, 2000, **104**, 8554–8556.
44 J. R. Swierk, N. S. McCool, T. P. Saunders, G. D. Barber and T. E. Mallouk, *J. Am. Chem. Soc.*, 2014, **136**, 10974–10982.